Effect of regular thicknesses on the microstructural and quantitative analysis for a hypo-eutectic ductile iron alloyed with Ni and V

E. Colin-García [a,*], R.G. Sánchez-Alvarado [a], A. Cruz-Ramírez [b], M.A. Suarez-Rosales [c], L. Portuguez-Pardo [a], J.C. Jiménez-Lugos [a]

[a.] Instituto Politécnico Nacional – ESIQIE, Departamento de Ingeniería en Metalurgia y Materiales, Ciudad de México, México
[b.] Instituto Politécnico Nacional – UPIIH, Departamento de Ciencias Básicas, Hidalgo, México
[c.] Universidad Autónoma Metropolitana – UAM-Azcapotzalco, Departamento de Materiales, Ciudad de México, México
* Correspondence: ecoling1400@alumno.ipn.mx

(Received 14 November 2023; Accepted 10 January 2024)

Abstract

Ductile iron contains free graphite nodules inside the metallic matrix, which generally consists of ferrite and pearlite in the as-cast condition. The casting thicknesses greatly influence on the size, shape, and quantity of the microconstituents of the metallic matrix and the graphite nodules and, therefore, on the mechanical properties. This investigation studied the cooling rate (imposed by the casting thicknesses) on the metallic matrix and the nodular characteristics of a ductile iron low alloyed with 0.8 %Ni and 0.15 %V. The ductile iron was manufactured by the sandwich technique with ladle inoculation. Six plates of different thicknesses, from 4.3 mm to 25.4 mm, were fabricated in a green sand mold. The microstructural characterization was performed by optical microscopy (OM), scanning electron microscopy (SEM), and the image J software by applying different quantification methods. The area method to obtain the average nodule size and nodularity provided more reliable results than the perimeter and total particle count methods. The hardness test on the Rockwell C scale carried out the mechanical characterization. The low content of vanadium added to the ductile cast iron had a negligible effect on the solidification pattern, mainly due to the graphitizing impact of the nickel and silicon addition. Thus, the microstructural features results are primarily due to the cooling rate imposed by the casting thickness. The thinnest casting section significantly improves the nodule count (414 Nod/mm^2), sphericity (0.96), and nodularity (96.21 %). In contrast, the thickest casting plate obtained the highest volume fraction of graphite (10.85 %) and the lowest volume fraction of undesirable particles (0.36 %). The high cooling rate in the thinnest casting plate obtained the highest hardness of 31.56 HRC because of the higher contents of the volume fraction of pearlite (33.7 %) and carbides (4.5 %).

Keywords: *Ductile iron; thickness; microstructure; cooling rate; quantitative analysis; nodular characteristics*

1. Introduction

The ductile cast iron or ductile iron (DI), also called spheroidal or nodular iron, contains free graphite with spheroidal shape (nodules) inside a metallic matrix. This material presents high mechanical properties attributed to the graphite morphology, which avoid and prevent the tendency to formation or propagation of cracks [1,2].

The cooling rate and the alloying elements of ductile iron modify the graphite nodules (morphology, quantity, distribution, or size) and phases or microconstituents of the metallic matrix [3]. The cooling rate imposed by the casting thickness has a substantial impact on the formation of nodules; it has been reported the formation of 2770 nod/mm^2 for a plate thickness of 1.9 mm [4]; this is a higher nodule count than those obtained in standard Y-block samples of 25.4 mm with 225 Nod/mm^2 [5]. Thus, the thicknesses in ductile iron castings have been classified as thin wall ductile iron (TWDI), with casting sections less than 4 mm [6]. However, some authors point out that the minimum thickness to be considered as TWDI has yet to be established, and it could be considered as 3, 4 or 5 mm as a maximum value limit [6]. Heavy thickness or thick thickness castings consider large dimensional sections as 75 mm [7] or 300 mm [8]. Conventional walls in ductile iron castings have been referred to as "regular thickness" of ductile iron in the range between thin and thick wall ductile iron [9].

The morphology and amount of free graphite play an essential role in the microstructure and mechanical properties of ductile iron; these can be modified in samples having different thickness castings, such as crankshaft, due to changes in the cooling rate; as a result, it is necessary to characterize each thickness. The most common ways to analyze ductile iron are i) graphite particles considering number, size, and nodularity; these parameters of free graphite are known as "nodular features" [10] or nodular characteristics [11]. ii) The phases or microconstituents. However, a more specific and complete microstructural analysis in a ductile iron considers more significant number of nodular characteristics such as nodule count, total particle count, nodule size, interparticle distance, sphericity, nodularity, volume fraction of nodules, total particles, and undesirable particles together with the phases or microconstituents of the metal matrix as pearlite, ferrite, carbides and ferrite/pearlite ratio.

Two methods are currently used to obtain the nodular characteristics. The first is a comparative method that takes micrographs at 100X and compares them with representative images reported in the ASTM A 247 standard. The second method uses micrographs and specialized software to obtain results that are more exact; this method was denominated "quantitative analysis," whose objective is to get characteristics of the three-dimensional effect from measurements of two-dimensional objects on polished or etched metallic surfaces [12]. With the advancement of science, the results computed in 2-D can be employed in complex mathematical models that represent suitable results in 3-D [10]; this is an advance for researchers and science. However, at the industrial level, such as in the automotive sector, quantitative analysis in 2-D continues to be used for its components because more accurate results are obtained relatively quickly and without so many complications [13,14].

Quantitative analysis is widely used to characterize ductile iron with different alloying elements [15], the quality of ductile iron before austempering heat treatment [14], the phases obtained after hardening induction as industrial components [16] or studying nodular characteristics in thin or thick thicknesses [6,8]. Nevertheless, some investigators focus on a particular nodular characteristic due to the importance of nodular morphology inside ductile irons. Riposan I. [17] used two mathematical models according to ISO 945-4-219 and ISO 16112:2017 to assess the nodularity, concluding that the best nodularity result was obtained using the model of ISO 945-4-219. Sosa A.D. [18] studied the residual stress nodule count and distortion in TWDI plates having different metallic matrices, concluding that residual stress and distortion are highly affected by nodule count. Other authors have focused their studies on the effect of alloying elements on the metallic matrix. Colin Garcia E. [19] Studied the addition of nickel in three casting modulus of ductile iron. The results showed that nickel contributed to avoiding forming iron carbides and obtaining a high quantity of pearlite in the metallic matrix with small thicknesses. Sazegaran H. [20] studied the addition of aluminum and copper to the microstructure and morphology of graphite in ductile iron, concluding that increasing these alloying elements increased both the number of nodules and the volume fraction of pearlite and graphite while the nodularity decreased.

On the other hand, vanadium is a carbide stabilizer; its addition to the ductile cast iron increases the strength and hardness by an increase of the pearlite amount due to the formation of eutectic carbide that appears as slight white inclusions in the microstructure [14].

With the advancement of characterization techniques, new ways have been discovered to obtain more accurate results in the characterization of graphite and phases in the matrix, such as 3-D quantitative analysis of graphite morphology based on XRD [21] or analysis of the sphericity and spatial distribution of graphite nodules based on morphological tools

(mathematical models and imaging software) [22]. Due to their versatility, quantitative analysis of ductile iron continues using uncomplicated equations or mathematical models.
The mechanical characterization of ductile iron is mainly carried out in Y-Block castings to obtain samples as a tensile or compressive test, fatigue, impact, and hardness. However, it is a problem to evaluate different thicknesses in TWDI because the walls are too small to obtain samples for various mechanical tests; on the contrary, in thick thickness castings is necessary they require several samples to get an accurate result. A way to evaluate the changes of mechanical properties in ductile iron with different thicknesses is the hardness since this is very versatile and only requires a small section of the thickness to evaluate the change of microstructure concerning metallic matrix. The Rockwell C hardness is commonly used for this purpose.
The hardness of ductile iron is affected by three elements within the chemical composition: carbon, silicon, and phosphorous since these elements are related to a parameter called carbon equivalent (CE), which modifies the metallic matrix. The relation between the three elements is shown in Equation (1). Ductile irons with CE values less than 4.3 % are called hypo-eutectoid ductile iron; those having CE higher than 4.3% are called hyper-eutectic, while eutectic ductile irons present a CE of 4.3 % [23].

$$CE = \%C + \left(\frac{1}{3}\right)(\%Si + \%P) \qquad (1)$$

It is widespread in the literature to find investigations on the hyper-eutectic ductile irons because a high carbon equivalent improves some nodular characteristics, such as nodule count and nodule size, and it modifies the phases, increasing the hardness. However, an adverse effect is that sometimes nodules present excessive nodule size, losing sphericity. This work conducted a detailed study of the graphite features for a hypo-eutectic ductile iron low alloyed with 0.8 % Ni and 0.15 %V. It is expected that the nickel addition improves the nodule count and homogenizes the sphericity, while the vanadium increases the hardness of ductile iron due to the formation of carbides; despite, the nodule count and nodularity of graphite are decreased [19, 24]. In this sense, the research presents a deep analysis of the quantitative determination of the main graphite features by applying classical equations. The effect of six regular plate thicknesses (from 4.3 to 25.4 mm) was studied on the nucleation-growth of nodules and phases or microconstituents and its impact on the hardness.

2. Experimental procedures

2.1 Foundry of castings

A ductile iron alloyed with 0.8 % nickel and 0.15 % vanadium was produced in a coreless induction furnace medium frequency with 50 kg of capacity. The base iron melted was obtained using 35 % cast iron scrap, 30 % low carbon steel (1018), and 35 % pig iron in the temperature range between 1490 – 1520 °C. The metal base was adjusted to obtain the chemical composition through a high carbon riser as recarburizing, FeSi (75 %), high purity nickel, and FeV (75 %). The molten metal was inoculated with 1 % calcifer (75 %Si + 1 %Ca, 0.9 %Al, 1.1 %Ba) in the stream from the coreless induction furnace to the ladle, where it was nodulized at the same time with 1.5 % MgFeSi agent (45 %Si, 8 %Mg, 3.3 %Ca, 3 % Rare Earth) using the sandwich technique. The treated metal was poured at a temperature of 1450 ºC into green sand molds previously manufactured with a model pattern of six plates like the one shown in Fig. 1a. The molds were shaken out after 30 minutes of cooling. The

six plates of the model have the following dimensions: 120 mm in length, 40 cm wide and variable thicknesses of 4.3, 8.5, 12.7, 16.9, 21.1, and 25.4 mm. Fig. 1b shows the fabricated plates cut from the feeding system.

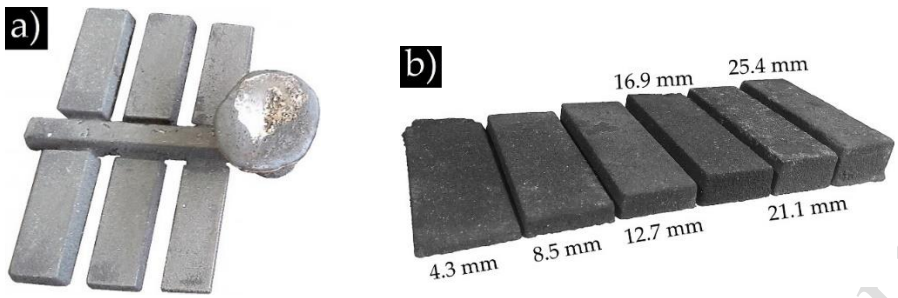

Figure 1. Model of the plates a) after casting and b) plates cut from 4.3 to 25.4 mm

The nominal chemical composition of DI was obtained employing an emission optic spectrograph (ARL Thermo scientific, 360 model, 4725-series). The measurement was made on three different plates to get the average composition.

2.2 Microstructural characterization

The rough surface for plates (approximately 1.5 mm) in contact with the molding sand, shown in Fig. 2a, was rectified to eliminate possible surface defects such as porosities or micro-shrinkages. They were cut along lines A-A' and B-B' according to Fig. 2b to obtain microstructural and hardness characterization specimens. Micrographs obtained in a light microscopy Olympus PMG-3 model carried out the microstructural characterization. In addition, EDS-SEM was used to determine the elements in the carbides, and images were taken in a scanning electron microscope, a JEOL model 6300. For the microstructural analysis, three micrographs at 100 magnifications (100X) were obtained for each point of a, b, c, d, and e, shown in Fig. 2b. Conventional metallographic procedures prepared the specimens: the roughing was performed using abrasive paper grades 180, 220, 320, 400, 600, and 1000, the polishing was carried out with Al_2O_3 powder with a size of 0.3 µm and the chemical etched was performed using two chemical reagents; nital 3% and ammonium persulfate 10 %.

Figure 2. Plate thickness of 12.7 mm a) surface in contact with green sand, and b) plate rectified.

2.3 Quantitative analysis of ductile iron

Quantitative analysis was made using the Image J software with a ratio of 1.11 pixels/microns and micrographs at 100X on polished condition to obtain nodular characteristics such as total particle count, nodule count, nodule size, sphericity, nodularity, interparticle distance, the

volume fraction for graphite of total particles, graphite of nodules, and undesirable particles. These results were obtained considering 65 % of sphericity and minimum diameter size of 10 µm [25], referred to regular thickness of ductile iron. Furthermore, ferrite and pearlite volume fractions were obtained on micrographs with nital etched conditions, while the volume fraction of carbides with ammonium persulfate was on etched conditions.

2.4 Hardness

Rockwell C hardness measurements were obtained by applying 150 kg of charge and a diamond tip indenter according to ASTM E 18. The indentations were performed on polished surface samples in a cross-section through a durometer Wilson 3T TBRB model. The average of 7 measurements and its deviation standard were reported for each plate thickness.

3. Results and discussion

3.1 Chemical Composition of ductile iron

The chemical composition of ductile iron alloyed with 0.8 % nickel and 0.15 % vanadium is shown in Table 1. Silicon promotes the formation of ferrite and it can suppress the formation of carbides [26]. Manganese is strongly pearlite-forming in high levels, leading to the formation of carbides in grain boundaries. In addition, manganese segregation delays the stability of super-cooled austenite and obstructs the graphite nodulizing process [27]. Therefore, a manganese content of less than 0.3% is preferable if the casting has a thin thickness and a heat treatment will be applied [28]. The residual magnesium content in ductile irons should be 0.02 - 0.05 % to obtain a correct spheroidal graphite [29]. Nickel is a graphitizing element [19], while vanadium is a carburizing element [30].

Table 1. Chemical composition of ductile iron alloyed with nickel and vanadium (wt%).

C	Si	Mn	P	S	Mg	Ni	V	Cu	Cr	Mo	Ti	Sn	Pb	Al	As	CE
3.0	3.34	0.35	0.014	0.003	0.03	0.85	0.15	0.12	0.05	0.008	0.006	0.07	0.01	0.02	0.003	4.11

The carbon equivalent (CE) was obtained using Equation (1) with elements showed in Table 1. The CE result was 4.1, which corresponds to a hypo-eutectic ductile iron. CE is a solid parameter to consider in ductile iron castings; this indicates the solidification path to determine the first phase to solidify modifying nodular characteristics. Fatahalla N. [31] reported that hyper-eutectic DI shows a higher nodule count than hypo-eutectic DI. This behavior is because in hyper-eutectic DI the first phase to nucleate and grow is graphite [32].

3.2 Microstructural characterization of ductile iron

The ductile iron micrographs on polished condition of the six plates with different thicknesses from 4.3 mm to 25.4 mm are shown in Fig. 3. It is shown from the micrographs that increasing thickness, the number of nodules decreases while the size of the nodules is increased. The plate thickness of 4.3 mm presented the highest number of graphite nodules and the smallest size, while the plate thickness of 25.4 mm presented the opposite behavior, with the highest nodule size and the lowest nodule count. The six plate thicknesses presented a uniform distribution of nodules with good nodularity; however, a lower sphericity is evident in larger graphite nodules such as those formed in the 21.1 mm and 25.4 mm thicknesses plates.

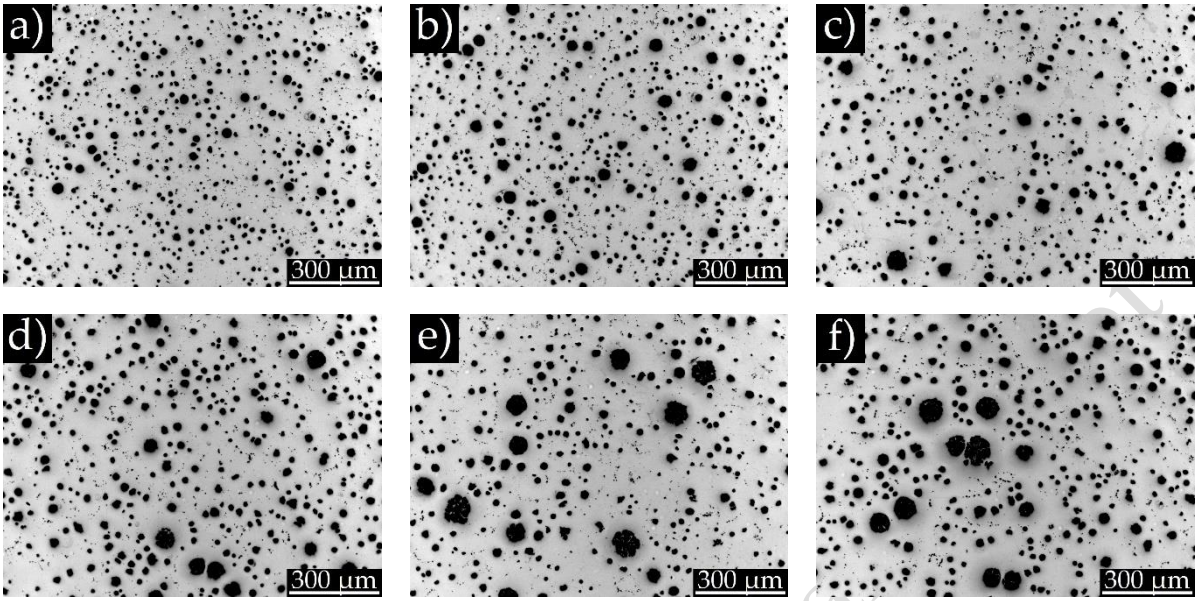

Figure 3. Micrographs on polished condition for plate thickness a) 4.3, b) 8.5, c) 12.7, d) 16.9, e) 21.1, and f) 25.4 mm.

Fig. 4 shows that the microstructures of the six plate thicknesses contain graphite nodules immersed in a metallic matrix composed of a mixture of pearlite and ferrite. When the thickness of the plates decreases, the amount of pearlite increases as observed in the plates with thicknesses of 8.5 mm and 4.3 mm. The higher cooling rate obtained in the small plates favored pearlite formation. On the other hand, slow cooling rates, as recorded in the larger plates with thicknesses of 12.7 mm - 25.4 mm favored the formation of ferrite.

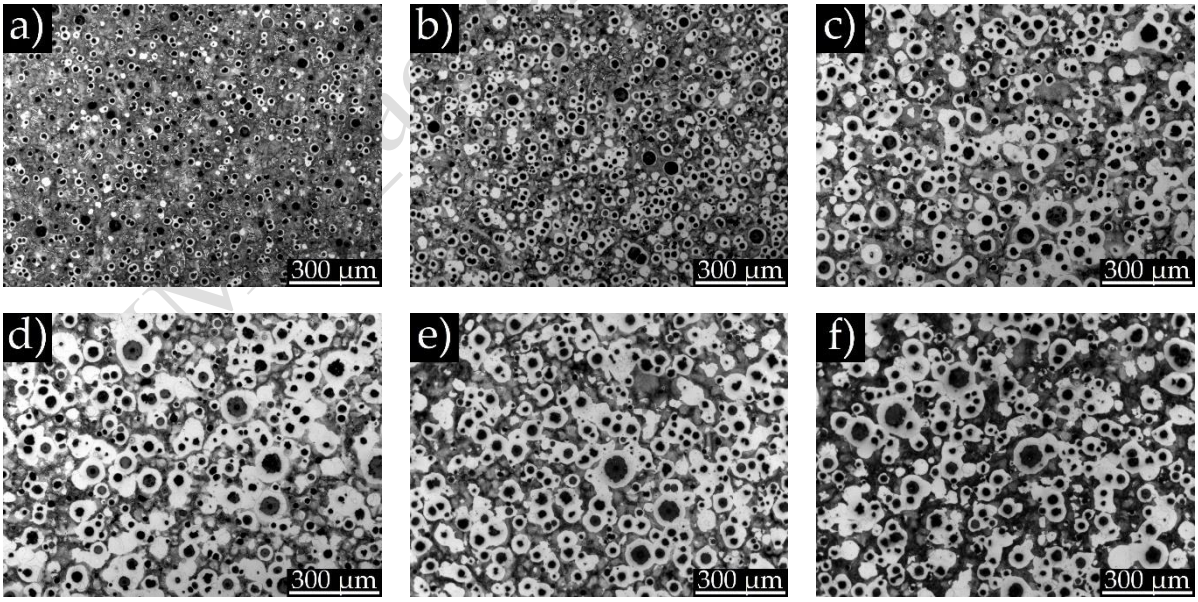

Figure 4. Micrographs at nital etched condition for plate thickness a) 4.3, b) 8.5, c) 12.7, d)16.9, e) 21.1 and f) 25.4 mm.

The ferrite and carbide phases present similar white tonality inside the metal matrix, so performing a quantitative analysis using Image J software to determine each amount is tough.

Therefore, an etch with ammonium persulfate at 10% was performed to darken the metallic matrix, revealing the carbides in a bright white color [33]. Fig. 5 shows the presence of the carbides formed in the six plates of different thicknesses from 4.3 to 25.4 mm. The largest amount of carbides was formed at a plate thickness of 4.3 mm, which decreases until a plate thickness of 12.7 mm. The carbides are not developed for thicker thickness ranges from 16.9 to 25.4 mm.

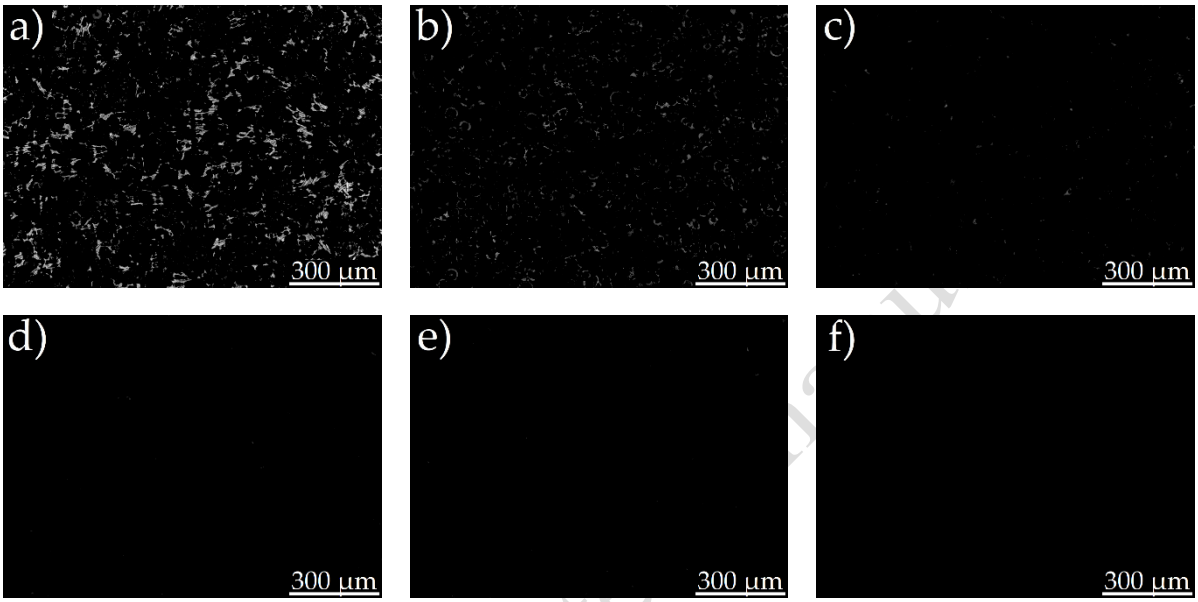

Figure 5. Micrographs at ammonium persulfate etched for plate thickness a) 4.3, b) 8.5, c) 12.7, d) 16.9, e) 21.1, and f) 25.4 mm.

3.3 Quantitative analysis of ductile iron

3.3.1 Nodule count and total particle count

During the solidification of ductile iron, two types of graphite particles can form; the first one is the graphite nodules, and the second one is irregular graphite shapes such as vermicular or hemispherical particles. Based on this classification, there are two ways to quantify the graphite particles. 1) Nodule count. The number of graphite nodules in a micrograph is expressed as Nod/mm^2. 2) Total particle count. The total number of graphite particles, including irregular graphite shapes and nodules [34], is expressed as Part/mm^2. Identifying the graphite particles is essential because some nodular characteristics are strictly computed through nodule count, while others are with total particle count.

The nodule count and total particle count for ductile iron with plate thickness ranging from 4.3 to 25.4 mm are shown in Fig. 6. In both cases, the counts decrease with increasing plate thickness with the highest values obtained at the plate thickness of 4.3 mm being 414 Nod/mm^2 and 428 Part/mm^2, respectively. It is evident that the total particle count is higher than the nodule count; the gap that separates each point of the curves for the same plate thickness is the count of the irregular graphite shapes. In this case, both curves are very close because ductile iron shows only a few irregular graphite particles within a larger number of nodules; however, the curves can diverge strongly in ductile iron containing a larger number of irregular graphite shapes. A high number of nodules is a suitable parameter of the quality

of ductile iron; the microstructure becomes finer and narrows the tendency to obtain chill carbides, and this refinement reduces the amount of misformed graphite [35].

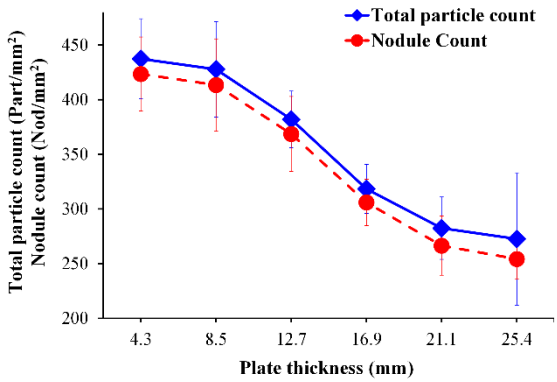

Figure 6. Nodule count and total particle count for plate thickness from 4.3 to 25.4 mm.

In the hypo-eutectic ductile irons, the first phase in growth is the austenite with a dendritic morphology (austenite proeutectic). The crystals' nucleation occurs at the mold wall and the inner melt that originates columnar grains. During the formation of austenite, the carbon atoms are expelled into the remaining liquid until eutectic composition is obtained; from this point, the liquid is transformed into two types of solids depending on whether solidification follows the metastable reaction (carbides) or eutectic (graphite nodules) [36]. The growth of graphite nodules in the molten metal begins in the particles added in the nodulizing and inoculant agents (magnesium, calcium, or cerium covered by a thin layer of magnesium silicate), which act as heterogeneous nucleation sites [37]. During this stage, many nuclei are formed to precipitate graphite. Initially, these particles do not serve as nucleation sites for graphite because their crystalline structure is not coherent with that of graphite. At the end of the inoculation process, these particles change due to the formation of layers of other silicates and oxides of the inoculating elements. The silicates have the same hexagonal structure as graphite, thus serving as effective nucleation sites for the growth of graphite nodules [38].

Various graphite particle counts can be achieved with different solidification cooling rates imposed by each plate thickness, as shown in Fig. 6. The highest particle and nodule counts were obtained in the plate with a thickness of 4.3 mm, while the lowest nodule count was obtained in the plate with thickest thicknesses of 25.4 mm. Górny M. [39] reported a similar behavior, quantifying the highest number of nodules in the small plate of 2 mm, where the highest solidification rates were obtained, and the lowest number of nodules in the plate with a thickness of 15 mm. This behavior can be explained in terms of undercooling. The theory of heterogeneous nucleation states shows that for a given substrate, nucleation is instantaneous when a specific undercooling is reached. The number of active nuclei increases at large undercoolings caused by high solidification rates because the highest particle and nodule counts were obtained in the thinnest plates [40]. Another critical factor to consider about the number of graphite nodules and particles is the alloying elements, such as nickel and silicon, which are graphitizing elements that reduce the solubility of carbon in the molten metal and increase the number of ductile iron nodules [41,42].

3.3.2 Nodule size

The nodule size expresses the diameter of each graphite nodule in microns (µm). The calculation of this nodular characteristic considers a minimum size of 10 µm for regular thicknesses, while in TWDI the minimum size is 5 µm [43]. Strictly, the nodule size should not consider irregular graphite shapes such as vermicular, graphite flakes or hemispherical particles (less than 65 % sphericity) because, by definition, these particles have no diameter. Two methods can be used to obtain the average size of the graphite nodules.1) Area and 2) perimeter using the Equations (2) and (3), respectively.

$NS_{avg} = (2)\left(\sqrt{A\pi^{-1}}\right)$	(2)
$NS_{avg} = P\pi^{-1}$	(3)

P is the perimeter and A is the area, both for particles considered nodules.

Table 2 shows the values of the average nodule size using the area and perimeter methods in six plates with different thicknesses. Both methods were performed using the Image J software. It is noted that the average nodule size is very close and similar for both methods, obtaining the maximum difference of 0.65 µm in plate thickness of 12.7 mm, which represents less than 1 µm. In this study, the average nodule size is very similar because the plates tested have a constant thickness. However, the authors noted in previous studies that in samples with different thicknesses, such as Cr-alloyed camshafts, the average nodule size varied up to 7 µm, being higher in the method of the perimeter.

Table 2. Average nodule size by perimeter and area methods for plate thickness from 4.3 to 25.4 mm.

Nodule size Method	**4.3 mm**	**8.5 mm**	**12.7 mm**	**16.9 mm**	**21.1 mm**	**25.4 mm**
Perimeter (µm)	15.09 ± 0.58	17.28 ± 1.11	20.68 ± 1.08	21.98 ± 1.02	22.17 ± 1.64	24.33 ± 1.27
Area (µm)	15.30 ± 0.67	17.42 ± 1.16	20.03 ± 1.44	21.67 ± 1.04	22.41 ± 1.78	24.17 ± 1.37
Difference (µm)	0.21	0.14	0.65	0.31	0.24	0.16

Although the two methods are reliable for obtaining the average nodule size, there are some significant differences. Fig. 7 shows a graph with the nodule size distribution of area and the perimeter methods for plate thickness of 4.3 mm measured in one micrograph corresponding to points a, b, and c shown in Fig. 2b. It is evident that the nodule size by the perimeter method starts with a size of 9 µm (3 nodules), and ends at 31 µm (3 nodules) having a more irregular distribution. In contrast, the area method starts at 10 µm and ends at 30 µm. This behavior means that the perimeter method includes particles below the limit considered as a nodule and obtains a larger nodule size than the area method. Therefore, the area method will be used in this study to report the average nodule size, ensuring a minimum size of 10 µm.

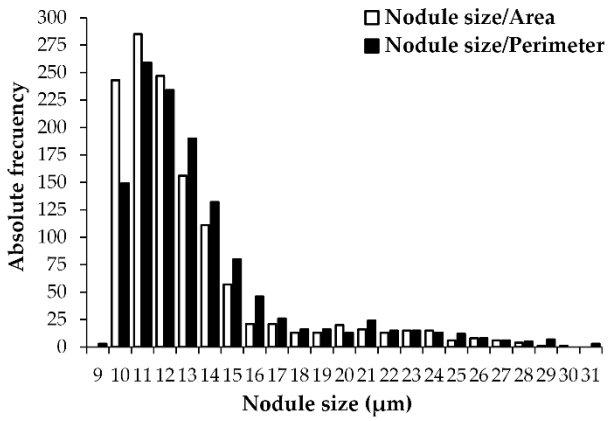

Figure 7. Distribution of nodule size for plate thickness of 4.3 mm through area and perimeter method.

The nodule size distribution for each plate thickness from 4.3 mm to 25.4 mm is shown in Fig. 8. The plate thickness of 4.3 mm shows the smallest nodule size with a maximum absolute frequency for the size of 10 µm; after the ultimate value, the absolute frequency begins to decrease homogenously up to a nodule size of 39 µm. As the thickness of the plates increases, the nodule size increases, and the number of nodules decreases. Therefore, the maximum frequency changes from left to right, obtaining fewer small nodules in plate thickness of 25.4 mm with more nodule size distribution.

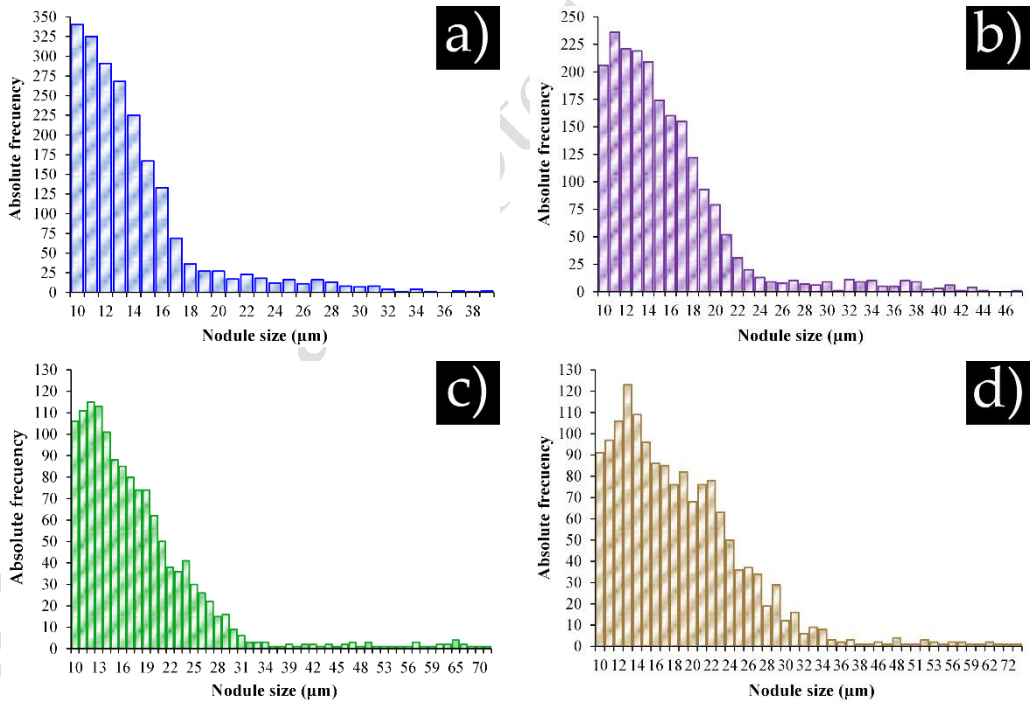

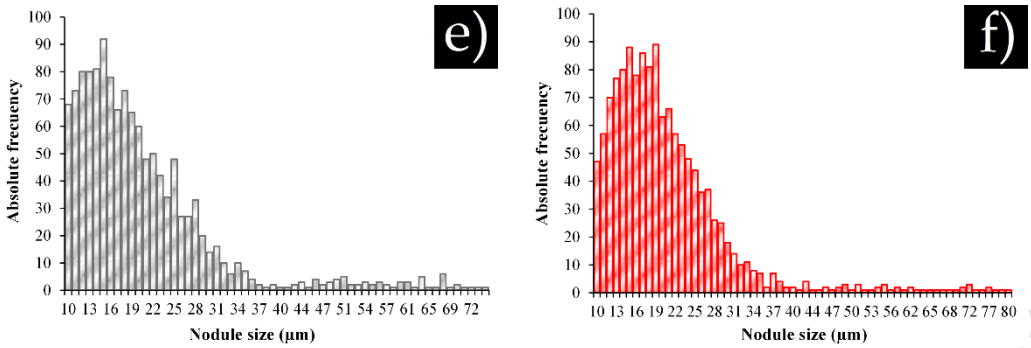

Figure 8. The Nodule size distribution of plate thickness of a) 4.3, b) 8.5, c) 12.7, d) 16.9, e) 21.1, and f) 25.4 mm.

The liquid-phase carbon precipitates in the form of graphite nodules when the eutectic temperature is reached. Graphite nodules nucleate and grow freely for a short period through the depletion of carbon atoms in the liquid state. Hence, the austenite nucleates around the graphite nodules due to the low carbon concentration in shell form (austenite surrounds the nodules) and coarse, forming eutectic cells (EC). During eutectic solidification, only the austenite is in contact with the liquid, and carbon diffusion through the austenite shell is the mechanism that controls the nodule growth [44,45]. Eventually, different eutectic cells will encounter primary dendrites forming an austenite network with nodules inside and trapping the newly formed nodules [36]. The first nucleated nodules grow more than the last ones, so the liquid decreases until the eutectic solidification ends. The continuous drop in temperature initiates graphitization in the solid state; during this period, the high carbon austenite expels carbon atoms and continues its diffusion into pre-existing graphite nodules until the austenite acquires a eutectoid composition [44]. As mentioned, the nodule size is affected by the cooling rate imposed by the thickness of the plates during solidification. In small plate thicknesses as 4.3 and 8.5 mm, where the fastest solidification and graphitization occurred, the nodules presented a lower size distribution than those obtained in higher plate thicknesses (21.1 and 5.4 mm). Another essential factor to consider is that the addition of Ni close to 0.8% refines the size of the graphite nodule, and its distribution in the microstructure is more homogeneous [19].

3.3.3 Interparticle distance

The nodule count and the average nodule size are related through a parameter known as interparticle spacing (λ_G) ; this nodular characteristic represents the carbon diffusion distance. It is necessary to consider that the average nodule size should not consider the irregular shapes of the graphite since, by definition, they do not have a diameter. The interparticle distance is obtained using Equation (4) [25].

$$\lambda_G = (55.4)\left(\frac{NS_{avg}}{Nodule\ count}\right)^{\frac{1}{3}} \quad (4)$$

NS_{avg} is the average nodule size in µm, and nodule count is expressed as Nod/mm^2.

The interparticle spacing measured on plates of different thicknesses from 4.3 to 25.4 µm is shown in Fig. 9. It can be seen that the interparticle spacing is more significant when the nodule size increases and when the number of nodules is low. The shortest interparticle spacing (18.23 µm) was obtained at the plate thickness of 4.3 mm due to the high cooling

rate, while the longest value of 25.33 µm was obtained at the plate thickness of 25.4 mm due to the low cooling rate.

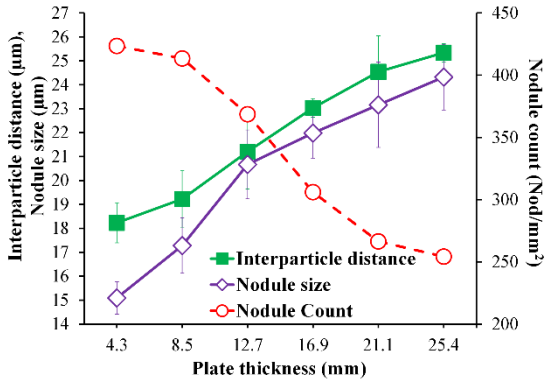

Figure 9. Interparticle distance for plate thickness from 4.3 to 25.4 mm.

3.3.4 Sphericity and nodularity

Sphericity and nodularity can sometimes be confused; however, both have different meanings. Sphericity refers to the roundness of the nodules in a range of 0.65 to 1.0. These parameters were described by Ruxunda R.E. [25] according to a widespread convention in industrial companies (Image pro-plus, Omnimet Enterprise handbook, and UTHSCSA Image tool Handbook). The lower limit refers to the minimum roundness accepted to be considered as a nodule, while the higher limit refers to a perfect circle. Sometimes, the minimum sphericity accepted is different [17], and some researchers reported this characteristic as % [46]. The sphericity for this research was obtained using the perimeter and area through the sphericity shape factor shown in Equation (5) [47]. However, more equations exist to get this nodular characteristic [48]

$$SSF = \frac{4 \cdot \Pi \cdot Area}{(Perimeter)^2} \quad (5)$$

Nodularity represents the percentage ratio for acceptable particles area (graphite of nodule count) to graphite of acceptable plus unacceptable particles area (total particle count) expressed in %. Equation (6) [25] shows the standard model used. Nevertheless, sometimes nodularity is reported as a percentage of the nodule count and total particle count according to Equation (7) [49] or using other mathematical models reported in ISO standards [17].

$$\%\,Nod = \left(\frac{Area\ of\ nodule\ count}{Area\ of\ total\ particles\ count}\right) X100 \quad (6)$$

$$\%\,Nod = \left(\frac{Nodule\ count}{Total\ particles\ count}\right) X100 \quad (7)$$

Fig. 10 shows the sphericity decreases with increasing plate thickness, obtaining values of 0.9 to 0.86 for plate thicknesses of 4.3 mm and 25.4 mm, respectively. The higher cooling rate imposed by small thicknesses such as 4.3 mm contributes to improving the sphericity close to 1.0, while at larger thicknesses, the graphite nodules are far from being a perfect circle for the trials developed using the same amount and type of nodulizer agent.

Since sphericity decreases, the nodularity comes down similarly due to these nodular characteristics being strongly related. The nodularity decreases for two methods computed:

area and count. The nodularity–area values in a range of 96.2 to 87.5 were lower than the nodularity–-count in a range of 96.81 to 93.25 % for plate thickness of 4.3 to 25.4 mm, respectively. The different size distribution of the graphite particles [45]; as the plate thickness increases, some particles are bigger, and consequently, the area increases, and the nodularity area decreases [11]. The sphericity and nodularity behaviors obtained in this research are similar to those reported by Bojarro J.M. [49] in ductile iron with different CE and thicknesses from 1.5 to 38.1 mm. However, Tomaran S. [50] reported that nodularity by count is slightly higher than the area method in three grades of ductile iron.

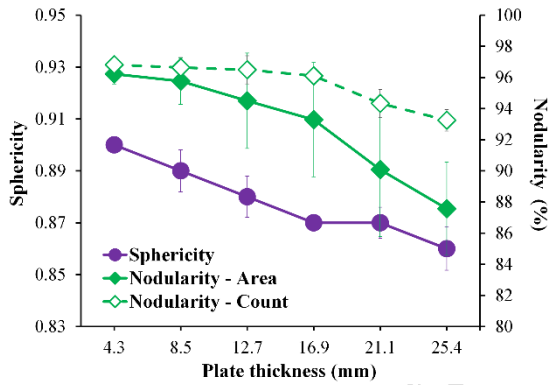

Figure 10. Sphericity and nodularity for plate thickness from 4.3 to 25.4 mm.

The plate thickness reduction decreases the average nodule size, improving the sphericity and nodularity [51]. This behavior is attributed to magnesium, rare earth, and the high cooling rate imposed by thickness.

During the manufacture of ductile iron, rare earth, and magnesium are added in molted metal through the modification stage (in this case, sandwich technique), generally in the range of 0.03 - 0.05 % to obtain graphite nodules. Anti-spheroidizing elements such as Ti, Bi, Zr, P, N, O, and S are surface-active elements that reduce the surface tension between graphite and liquid. The main surface-active elements, such as O and S, cause changes in the direction of the graphite growth on the A axis, resulting in an irregular graphite shape. The function of Mg and RE is to neutralize the two surface-active elements to obtain the growth of the carbon in Axis C and obtain a spherical shape [52].

During the solidification, the austenite dendrites interact with eutectic cells. Hence, the austenite thickness increases, and nodules grow; the uniformity of austenite thickness is increased when the time during the eutectic temperature increases, resulting in a non-uniform supply of atoms for nodular graphite in all directions [53]. Hence, in small plate thicknesses of 4.3 and 8.5 mm, the solidification and graphitization are very fast; therefore, the high nodularity initial is slightly lost. Furthermore, graphite nodules increase in size during the solid state, and nodularity decreases due to uneven diffusion of carbon atoms [53]. The final shape of the graphite depends mainly on the speed at which austenite envelops the nodules; this speed depends on the casting cooling and is influenced by the amount of magnesium [44]. Therefore, a small thickness requires less magnesium to form nodules, while a larger nodule requires more magnesium.

Alloying elements also influence the sphericity and nodularity. The addition of vanadium hurts nodularity, promoting the formation of chunky graphite in casting with long solidification times [54]. At the same time, nickel improves the sphericity and nodularity [19].

3.3.5 Graphite of nodules, graphite of total particles and undesirable particles

Sometimes, the terms surface fraction and area fraction, among others, describe the amount of phase in a micrograph. The volume fraction is a term widely used that is technically correct because the results are determined by the number of picture elements or "pixels" in stereography or quantitative metallography. Volume, area, line, and point are related through equality; VV = AA = LL = PP expressed as % [12,55].

The volume fraction for graphite of nodules refers to the amount of graphite contained only in the nodules (sphericity and nodule size higher than 65 % and 10 µm, respectively). The total particle graphite includes irregular graphite shapes (higher than 10) and graphite nodules.

The volume fraction for graphite of nodules and graphite of total particles for plates thickness from 4.3 to 25.4 mm are shown in Fig. 11. Increasing the thickness, the volume fraction of graphite is higher from 6.31 to 10.85 % and 6.55 to 11.24 %, for nodule count and particle count, respectively. The gap that separates each point in the curve is the area of irregular graphite shapes.

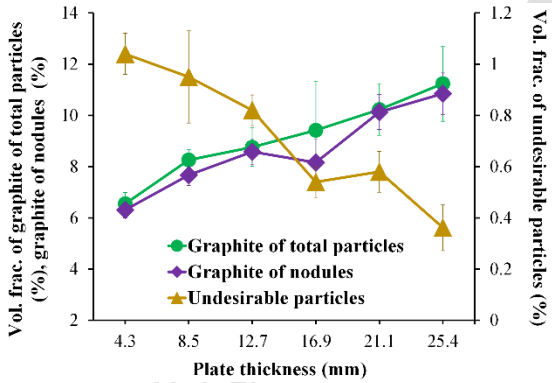

Figure 11. The volume fraction of graphite nodules, graphite total particles, and undesirable particles for plate thickness from 4.3 to 25.4 mm.

Hypo-eutectic DI generally presents a low volume fraction of graphite for nodules and total particles. The growth of graphite shapes (nodules or irregular shapes) increases the volume fraction; this depends on four stages: i) from the liquid, ii) during eutectic transformation, iii) during cooling eutectoid temperature and iv) during eutectoid transformation.

At the beginning of the solidification, austenite and graphite grow separately (divorced eutectic), leading to graphite particles that are in contact with the molten metal. At this point, the austenite dendrites grow, and then carbon is rejected to the interdendritic liquid, and thus viscosity increases, which restricts atomic movement.

After forming a certain amount of solid fraction, the dendrite coherency and graphite austenite interaction begin [56]. Afterward, the graphite phase is enveloped in a solid austenite shell; the carbon atoms expelled from austenite diffused on the surface of the nodules and irregular shapes, increasing the volume fraction of graphite. In plate thicknesses of 21.1 and 25.4 mm, the cooling rate is low, increasing the graphitization time, obtaining a larger volume fraction of graphite and graphite nodules, while graphitization in plate thickness of 4.3 mm is very short as a consequence, only a small volume fraction is obtained. The discarded particles computed during the volume fraction of graphite having a maximum size of 10 µm are commonly porosity, nonmetallic inclusions, pitting [22], micro-shrinkage, and small nodules; these are considered in the volume fraction of undesirable particles. This

characteristic is not always analyzed due to the low volume fraction presented on ductile irons. However, it is essential when applying austempering to DI because they should not exceed 1.0 % of porosity and micro-shrinkage and 0.5 % of carbides and non-inclusions [57]. The volume fraction of undesirable particles of ductile iron for plate thicknesses from 4.3 to 25.4 mm is shown in Fig. 11. The maximum number of undesirable particles is found in the plate thickness of 4.3 mm (1.04 %), which decreases when the thickness increases until plate thickness of 25.4 mm (0.36 %). This behavior is attributed to solid-state graphitization, where carbon atoms are ejected from the austenite. At this stage, only carbon atoms close to the surface of the nodules could diffuse towards them. In plate thickness of 4.3 mm, the fast-cooling rate could limit the diffusion of carbon atoms from the austenite to the graphite nodules, and then, these atoms nucleated in the form of nodules with an average size of less than 10 µm at the grain boundary of the austenite [53].

On the other hand, by having a greater plate thickness of 25.4 mm, the diffusion time is longer, so the atoms diffuse to the graphite nodules, avoiding nucleation at the grain boundaries, which reduces undesirable particles. These unwanted particles smaller than 10 µm (indicated within the red circles) are shown for plate thicknesses of 4.3 and 25.4 mm, as can be seen in Fig. 12. The most significant amount of graphite particles was found in the plate thickness of 4.3 mm, which decreases until the plate thickness of 25.4 mm. In addition, the most considerable volume fraction is attributed to small nodules and irregular graphite shapes.

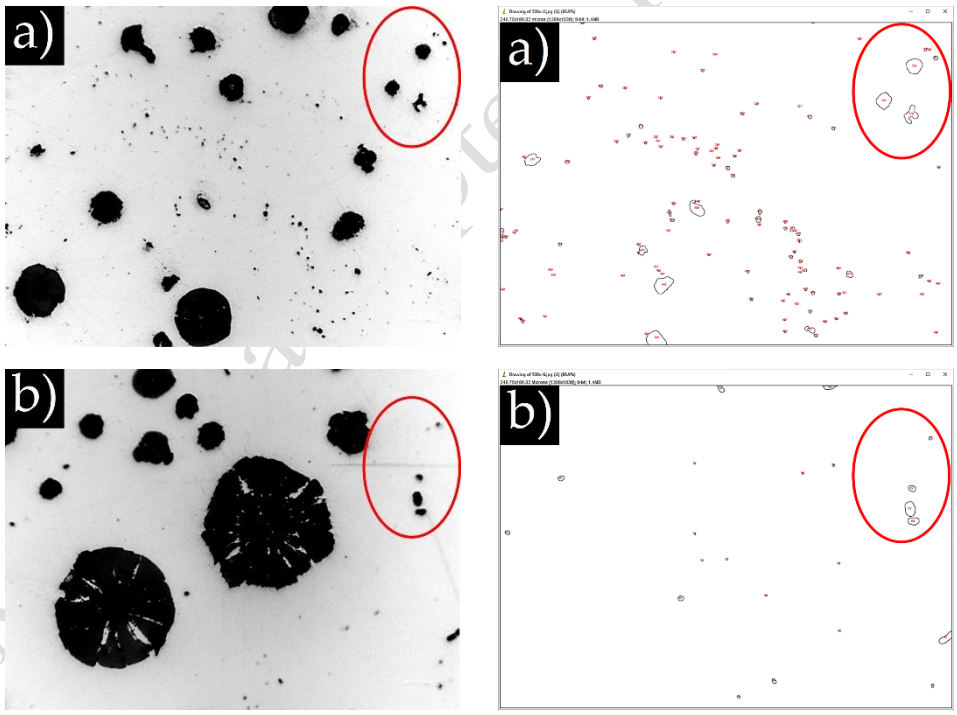

Figure 12. Graphite nodule size less than 10 µm for thickness a) 4.3 and b) 25.4 mm on polish condition analysed with Image J software.

3.3.6 Ferrite and pearlite

During the graphitization state, the austenite expels carbon until reaches the eutectoid composition so that the decomposition of austenite can lead to the formation of the ferrite phase if the stable reaction occurs (ferritic reaction) or the formation of ferrite and pearlite if

the metastable reaction occurs (pearlitic reaction). The eutectoid transformation depends on the competition between stable and metastable reactions, besides the cooling rate and the alloying elements [58].

Fig. 13 shows the volume fraction of ferrite, pearlite, and carbides of the six plates of different thicknesses. The volume fraction of ferrite increased with the increasing thickness of the plates, reaching the highest value (53.68%) for the plate thickness of 25.4 mm.

Ferrite is a phase obtained at a slow cooling rate; austenite continues expelling carbon atoms into nodules while the temperature descends. Ferrite usually nucleates at the nodule/austenite interface and grows symmetrically around the nodule, forming a halo. During the growth of the halo, the remaining austenite continues expelling carbon atoms to diffuse through the ferrite halo (ferrite reaction), which is thicker [59]. The cooling rate decreases when the plate thickness increases to 25.4 mm; the carbon diffusion time increases, obtaining more significant amounts of ferrite in the matrix [40], resulting in a decrement in pearlite [60].

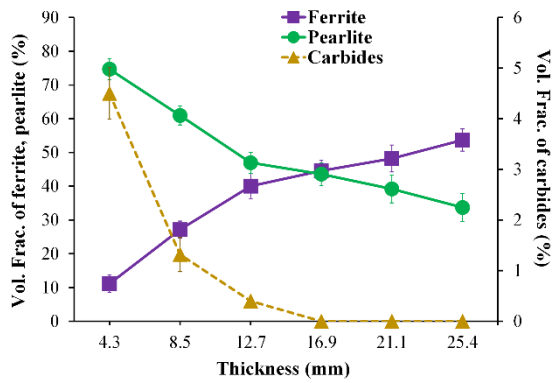

Figure 13. The volume fraction of phases and microconstituents for ductile iron from thickness 4.3 to 25.4 mm.

The pearlite presents an opposite behavior than ferrite. The volume fraction of pearlite increases when the casting plate decreases, obtaining the highest value (74.67 %) in plate thickness of 4.3 mm. When the ferrite halo is bigger enough, the diffusion of the carbon atoms through the ferrite gradually decreases. Hence, the temperature drop becomes low enough to nucleate the pearlite (pearlitic reaction).

The preferred nucleation site for the pearlite is the austenite/ferrite interface due to the carbon content in the austenite. However, pearlite grows faster than ferrite due to cementite and ferrite's cooperative (coupled) growth [59]. When the thickness is reduced to a plate thickness of 4.3 mm, the cooling rate increases the volume fraction of pearlite [40], and as a result, this microconstituent can nucleate at the austenite grain boundaries or the graphite/austenite interface.

3.3.7 Ferrite/Pearlite ratio

The volume fractions of ferrite and pearlite are significant to the mechanical properties of ductile iron, and they are related by the ferrite/pearlite ratio, which the cooling rate can modify.

Table 3 shows the volume fraction of ferrite and pearlite and the ferrite/perlite ratio for ductile iron obtained in the six plates of different thicknesses from 4.3 mm to 25.4 mm. The plate thickness, from 4.3 mm to 12.7 mm, had a ratio lower than 1.0 and is mainly constituted of a pearlitic matrix, which will increase the hardness and strength of the ductile iron.

If the ratio is higher than 1.0, as plate thickness is from 21.1 to 25.4 mm, ferrite is the predominant phase, so ductility and toughness increase.
A ferrite/pearlite ratio of 1.02 was determined for the casting plate of 16.9 mm; this ratio allows for obtaining an adequate balance between ferrite and pearlite and a good combination of mechanical properties.
The behavior of the ferrite/pearlite ratio obtained in this research is similar to that reported by Gonzaga R.A. [61], who reported that the as-cast DI having a 30/70 ratio presents higher Hardness than a 60/40 ratio.

Table 3. Ferrite/pearlite ratio for plate thickness from 4.3 to 25.4 mm.

Characteristic	4.3 mm	8.5 mm	12.7 mm	16.9 mm	21.1 mm	25.4 mm
Ferrite	11.13	27.16	40.04	44.57	48.22	53.68
Pearlite	74.67	60.95	46.97	43.6	32.9	33.7
Ferrite/pearlite ratio	0.15	0.44	0.85	1.02	1.23	1.60

3.3.8 Carbides

The volume fraction of carbides for a plate thickness from 4.3 to 25.4 mm is shown in Fig. 13. The amount of primary carbides (obtained during solidification) increases as the plate thickness decreases. In this case, the plate thickness of 4.23, 8.46, and 12.6 mm presented carbides, where the highest volume fraction (4.5%) was obtained in the plate thickness of 4.3 mm. The carbides were mainly concentrated in the middle of plates at points b, d, and e, as shown in Fig. 2b. Only a minimal amount of carbides was found near the perimeter.
The formation of carbides is attributed to different factors such as [62]; high cooling rate during the solidification, carbide-forming elements during the melting step, low CE, low Si content, inadequate or poor inoculation, excessive magnesium content, and a high superheat. In plates with small thicknesses, where high cooling rates are imposed, the solidification of ductile iron can occur wholly or partially according to the metastable phases diagram, which causes the transformation of the melt into ledeburite [63]. In Addition, the carbide content is increased by adding carburizing elements. During solidification, the inverse chill may occur, which is a segregation of carbide-forming elements such as manganese, vanadium, chromium, molybdenum, or titanium, increasing the concentration of these elements in the remaining liquid to solidify, promoting carbide formation. The formation of carbides is aided by increasing the concentration of these elements [64]. Although the morphology of carbides is irregular and complex, two distinctive shapes can be identified: plates and ledeburite shapes [63].
A scanning electron microscope (SEM) was employed to determine the elements inside carbide plates and ledeburitics. Fig. 14 shows an SEM micrograph and its punctual analysis in carbides. Fig. 14a shows carbide plates and regions of ledeburite transformed. Fig. 14b shows two points with a chemical composition; this presents a homogeneous distribution and similar main elements, such as carbide forming, such as V, Mn, and C.

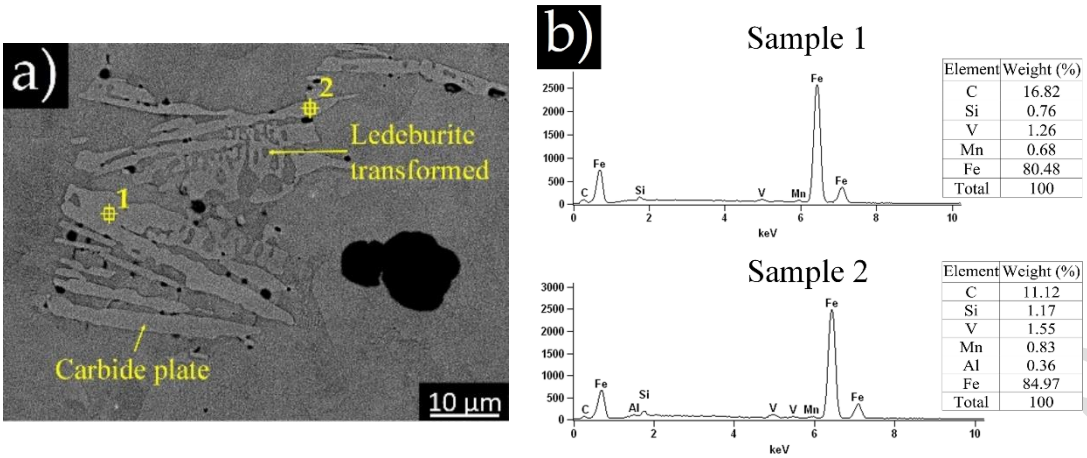

Figure 14. a) SEM micrograph and b) Punctual X-ray microanalysis of the ductile iron.

Adding nickel and silicon elements together with a low cooling rate prevents carbide formation in plate thickness from 16.9, 21.1, to 25.4 mm. Silicon delays the carbide formation [41]. Nickel shows a beneficial effect on solidification due to the reduction of the carbon content on the eutectic; the interval between γ-graphite and γ-Fe_3C transformation is increased, which suppresses the carbide formation, and therefore, nickel prevents a chill tendency [65].

It has been reported [64] that the vanadium addition for contents higher than 0.2 % to ductile iron affects the nodule count and nodularity by the carbide formation. However, the low content of vanadium added for the ductile cast iron had a negligible effect on the solidification pattern, mainly due to the graphitizer impact of the nickel and silicon addition. The graphite features, and phase results obtained are related to the effect of the cooling rate imposed by the different thicknesses evaluated.

3.4 Hardness of ductile iron

The hardness values on the Rockwell C scale for ductile iron on plate thickness from 4.3 to 25.4 mm are shown in Fig. 15. The hardness is greater when the plate thickness decreases, this behavior depends on the phases and microconstituents within the metallic matrix. These are obtained from the cooling rate imposed by the thickness during the solidification. As expected, low values of the ferrite/pearlite ratio present higher hardness, such as plate thickness from 4.3 to 12.7 mm, while higher values of the pearlite/ferrite ratio show a low hardness like thicknesses of 21.1 and 25.4 mm.

The correct balance of the ferrite/pearlite ratio with a hardness of 19.83 HRC was obtained in the plate thickness of 16.9 mm. The maximum hardness (31.56 HRC) was obtained in the plate thickness of 4.3 mm, which contains the highest volume fraction of pearlite and carbides. It has been reported that hardness is increased by adding carburizer elements such as vanadium or chromium because both contribute to obtain a higher volume fraction of carbides [24,66].

On the other hand, the minimum hardness (17.33 HRC) was found in plate thickness of 25.4 mm, this was attributed to the highest volume fraction of ferrite and graphite, both considered soft phases in ductile iron [67]. The results on hardness and its behavior when varying the thickness of the plates are similar to those reported by Guzel E. [68], who has worked with plates thicknesses ranging from 12.7 to 76.2 mm.

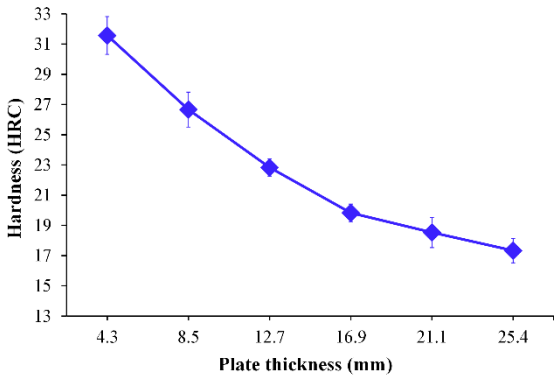

Figure 15. Rockwell C hardness for plate thickness from 4.3 to 25.4 mm.

It must be mentioned that the accuracy of results depends on the region analyzed. Therefore, a representative area of the ductile iron sample must be considered to get reliable results during the measurements of the phases or microconstituents and nodular characteristics, to obtain the most data information possible, and get a correct distribution of results [55]. Another source of error in the quantification is obtaining incorrect micrographs due to wrong metallographic preparation of the sample. Thus, adequate metallographic procedures must be applied [69] to get high-quality micrographs that increase quantification accuracy.

4. Conclusions

The nodular characteristics, phases, or microconstituents and their relation with the cooling rate imposed by different casting thicknesses were deep analyzed in a hypo-eutectic ductile iron alloyed with 0.8 % Ni and 0.15 % V. The results are summarized as follows:

1. The cooling rate imposed by different thicknesses casting modifies the nodular characteristics, phases, microconstituents, and hardness strongly.
2. The area method to obtain the average nodule size and nodularity provides more reliable results than the perimeter and total particle count methods.
3. The nodular features of nodule count, sphericity, and nodularity are improved when the casting thickness is decreased. The casting plate of 4.3 mm allows obtaining the highest nodule count of 414 Nod/mm^2, a sphericity of 0.96 and nodularity of 96.21 %. In contrast, the highest volume fraction of graphite and the lowest volume fraction of undesirable particles were obtained for the thickest casting plate.
4. The low content of vanadium added to the ductile cast iron had a negligible effect on the solidification pattern mainly due to the graphitizer effect of the nickel and silicon addition.
5. The higher volume fraction of carbides was obtained for the thinner casting plate due to the high cooling rate during solidification. The carbide formation was suppressed for the casting plate thicknesses from 16.9 to 25.4 mm due to a decrease in the cooling rate and the effect of the nickel and silicon addition.
6. The highest hardness of 31.56 HRC was obtained in the casting plate thickness of 4.3 mm because of the higher contents of the volume fraction of pearlite and carbides.

Acknowledgments

The authors wish to thank the Institutions CONAHCYT, SNI, COFAA, and SIP-Instituto Politécnico Nacional for their permanent assistance to the Process Metallurgy Group at ESIQIE-Metallurgy and Materials Department.

Author Contributions

Visualization, Software, and Writing - original draft, E. Colin-García; Data curation, E. Colin-García, M.A. Suarez-Rosales & R.G. Sanchez-Alvarado; Formal analysis, E. Colin-García & A. Cruz-Ramírez; Investigation, Eduardo Colin García & J.C. Jiménez-Lugos; Methodology, E. Colin-García & L. Portuguez-Pardo; Writing – review & editing, E. Colin-García, A. Cruz-Ramírez M.A. & Suarez-Rosales.

Data Availability Statement

Data will be made available on request

Conflicts of Interest

The authors declare no conflict of interest

References

1. T.J. Marrow, H. Çetinel, Short fatigue cracks in austempered ductile iron (ADI), Fatigue & Fracture of Engineering Materials & Structures, 23 (2000) 425-434. https://doi.org/10.1046/j.1460-2695.2000.00295.x
2. M.A. Neri, C. Carreño, effect of copper content on the microstructure and mechanical properties of a modified nodular iron, Materials Characterization, 51 (4) (2003) 219-224. https://doi.org/10.1016/j.matchar.2003.09.001
3. M. Persyk, A.W. Kochański, Prediction of ductile cast iron quality by artificial neural networks, Journal of Materials Research and Technology, 109 (2001) 305-307. https://doi.org/10.1016/S0924-0136(00)00822-0
4. E. Fraś, M. Górny, H. Lopez, Thin wall ductile iron castings as substitutes for aluminium alloy casting, Archives of Metallurgy and Materials, 59 (2) (2014) 459-465. https://doi.org/10.2478/amm-2014-0076
5. G. Rivera, R. Boeri, J. Sikora, Influence of the solidification microstructure on the mechanical properties of ductile iron, International Journal of Cast Metal Research, 11 (6) (1999) 533-538. https://doi.org/10.1080/13640461.1999.11819329
6. J.W. Soedarsono, T.P. Soemardi, B. Suharno, R.D. Sulamet-Ariobimo, Effects of carbon equivalent on the microstructures of thin wall ductile iron, Journal of Materials Science and Engineering, 5 (2011) 266-270
7. M. Ghoroghi, N. Varahram, Y. Perseh, Investigation into microstructure and mechanical properties of heavy section nickel alloyed austempered ductile iron in

accordance with austempering parameters, Material Design & Processing Communications, 3 (4) (2021) 5-11.
https://doi.org/10.1002/mdp2.220

8. J. Lacaze, S. Armendariz, P. Larrañaga, I. Asenjo, J. Sertucha, R. Suárez, Effect of carbon equivalent on graphite formation in heavy-section ductile iron parts, Materials Science Forum, 636-637 (2010) 523–530.
https://doi.org/10.4028/www.scientific.net/MSF.636-637.523
9. R.A. Martínez, R.E. Boeri, J.A. Sikora, Application of ADI in high strength thin wall automotive parts, 2002 World Conference on ADI, September 26-27, Kentucky, USA, 2002, 143-148.
10. B.I. Imasogie, U. Wendt, Characterization of graphite particle shape in spheroidal graphite iron using a computer-based image analyzer, Journal of Minerals & Materials Characterization & Engineering, 3 (1) (2004) 1-12.
https://doi.org/10.4236/jmmce.2004.31001
11. K. Davut, B. Çetin, E. Arslan, H. Meco, C. Yazganarikan, Nodularity and Nodule Count Analysis of Austempered Ductile Iron Castings by Digital Image Processing, 18th International Metallurgy and Materials Congress, 29 sept-01 oct, Istambul, Turkey, 2016, 497-500.
12. G. Das, Image analysis in quantitative metallography, Materials Characterization Techniques-Principles and Applications, 83(1007) (1999) 135-150.
13. C.A. Paredes-Orta, F. Manriquez-Guerrero, J. Torres-González, F. Castañeda, and I. R. Terol-Villalobos, Wear characterization of nodular cast iron based on clusters of nodules, Advanced Materials Research, 976 (2014) 184–188.
https://doi.org/10.4028/www.scientific.net/AMR.976.184
14. E. Colin García, A. Cruz Ramírez, G. Reyes Castellanos, J. Téllez Ramírez, A. Magaña Hernández, Microstructural and mechanical assessment of camshafts produced by ductile cast iron low alloyed with vanadium, Metals, 11 (146) (2021) 1–18.
https://doi.org/10.3390/met11010146
15. M. Górny, M. Kawalec, B. Gracz, M. Tupaj, Influence of cooling rate on microstructure formation of Si–Mo ductile iron castings, Metals, 11 (1634) (2021) 1-15.
https://doi.org/10.3390/met11101634
16. H. Ma, R.J. Bowers, D.O. Northwood, X. Sun, P.J. Bauerle, Residual stress and retained austenite in induction hardened ductile iron camshafts, WIT Transactions on Engineering Sciences, 76 (2012) 115–127.
https://doi.org/10.2495/TD120101
17. I. Riposan, D. Anca, I. Stan, M. Chisamera, S. Stan, Graphite Nodularity Evaluation in High-Si Ductile Cast Irons, Materials, 15 (7685) (2022) 1-21.
https://doi.org/10.3390/ma15217685
18. A.D. Sosa, M.D. Echeverría, O.J. Moncada, N. Míngolo, J A. Sikora, Influence of nodule count on residual stresses and distortion in thin wall ductile iron plates of different matrices, Journal of Materials Processing Technology, 209 (15-16) (2009) 5545–5551.

https://doi.org/10.1016/j.jmatprotec.2009.05.010
19. E. Colin-García, A. Cruz-Ramírez, G. Reyes-Castellanos, J.A. Romero-Serrano, R.G. Sánchez-Alvarado, M. Hernández-Chávez, Influence of nickel addition and casting modulus on the properties of hypo-eutectic ductile cast iron, Journal of Mining and Metallurgy, Section B: Metallurgy, 55 (2) (2019) 283–293. https://doi.org/10.2298/JMMB181012023C
20. H. Sazegaran, F. Teimoori, H. Rastegarian, and A. M. Naserian-Nik, Effects of aluminum and copper on the graphite morphology, microstructure, and compressive properties of ductile iron, Journal of Mining and Metallurgy, Section B: Metallurgy, 27 (1) (2021) 145–154. https://doi.org/10.2298/JMMB191224006S
21. C. Chuang, D. Singh, P. Kenesei, J. Almer, J. Hryn, R. Huff, 3D quantitative analysis of graphite morphology in high strength cast iron by high-energy X-ray tomography, Scripta Materialia, 106 (2015) 5–8. https://doi.org/10.1016/j.scriptamat.2015.03.017
22. L. A. Morales-Hernández, I.R. Terol-Villalobos, A. Domínguez-González, F. Manríquez-Guerrero, G. Herrera-Ruiz, Spatial distribution and spheroidicity characterization of graphite nodules based on morphological tools, 210 (2) (2010) 335–342. https://doi.org/10.1016/j.jmatprotec.2009.09.020
23. Foseco Ferrous Foundryman´s handbook (J.R. Brown), Butterworth Heinemann, Oxford, 2000, 32-34.
24. Ch.F. Han, Y.F. Sun, Y. Wu, Y.H. Ma, Effects of Vanadium and Austempering Temperature on Microstructure and Properties of CADI, Metallography, Microstructure, and Analysis, 4 (2015) 135–145. https://doi.org/10.1007/s13632-015-0197-1
25. R. E. Ruxanda, D.M. Stefanescu, T. S. Piwonka, Microstructure Characterization of Ductile Thin-Wall Iron Castings, AFS Transaction, 110 (2002) 1-17.
26. S.K. Putatunda, Influence of austempering temperature on microstructure and fracture toughness of a high-carbon, high-silicon and high-manganese cast steel, Materials & Design, 24 (6) (2003) 435–443. https://doi.org/10.1016/S0261-3069(03)00090-6
27. L. Rao, W.W Tao, S.J. Wang, M.P. Geng, G.X. Cheng, Influence of the composition ratio of manganese and copper on the mechanical properties and the machining performance of ductile iron, Indian Journal of Engineering and Materials Sciences, 21 (5) (2014) 573-579.
28. S. Dhanasekaran, A. Vadiraj, G. Balachandran, M. Kamaraj, Mechanical behaviour of an austempered ductile iron, Transactions of The Indian Institute of Metals, 63 (2010) 779-785. https://doi.org/10.1007/s12666-010-0119-5
29. A.S. Darmawan P.I. Purboputro, A. Yulianto, A.D. Anggono, W. Wijianto, M. Masyrukan, R.D. Setiawan, N.D. Kartika, Effect of magnesium on the strength, stiffness and toughness of nodular cast iron, Materials Science Forum, 991 (2020) 17–23.

https://doi.org/10.4028/www.scientific.net/MSF.991.17
30. G.M. Goodrich, Cast iron microstructure anomalies and their causes, AFS Transactions, 105 (1997) 669–683.
31. N. Fatahalla, H. Abd Al Hakim, A. Abo-El-Ezz, M. Mohamed, Effect of the percentage carbon equivalent on the nodule characteristics, density and modulus of elasticity of ductile cast iron Journal of Materials Science, 31 (18) (1996) 4933–4937. https://doi.org/10.1007/BF00355883
32. E. Moumeni, C.C. Tutum, N.S. Tiedje, J. H. Hattel, Analysis of nucleation modelling in ductile cast iron, IOP Conference Series: Materials Science and Engineering, January 01, Aachen, 2011. 1-7. https://doi.org/10.1088/1757-899X/27/1/012062
33. D.I. Pedro, R.C. Dommarco, Rolling contact fatigue resistance of Carbidic Austempered Ductile Iron (CADI), Wear, 418–419 (2018) 94–101. https://doi.org/10.1016/j.wear.2018.11.005
34. A.M. Herrera Navarro, H. Jiménez Hernández, H. Peregrina-Barreto, F. Manríquez Guerrero, I.R. Terol Villalobos, Characterization of the roundness degree of graphite nodules in ductile iron A new discrete measure independent to resolution, Superficies y vacío, 26 (2) (2013) 58-63.
35. Mr. Bahubali, B. Sangame, M. Vasudev, D. Shinde, The Effect of inoculation on microstructure and mechanical properties of ductile iron, Journal of Mechanical and Civil Engineering, 5 (6) (2013) 17-23.
36. R. Lora, A. Diószegi, L. Elmquist, Solidification study of gray cast iron in a resistance furnace, Key Engineering Materials, 547 (2011) 108–113. https://doi.org/10.4028/www.scientific.net/KEM.457.108
37. N.G. Kok Long, H. Sasaki, H. Kimura, T. Yoshikawa, M. Maeda, Heterogeneous nucleation of graphite on rare earth compounds during solidification of cast iron, ISIJ International, 58 (1) (2018) 123–131. https://doi.org/10.2355/isijinternational.ISIJINT-2017-398
38. A. de Albuquerque Vicente, J.R. Sartori Moreno, T.F. de Abreu Santos, D.C. Romano Espinosa, J.A. Soares Tenório, Nucleation and growth of graphite particles in ductile cast iron, Journal of Alloys and Compounds, 775 (2019) 1230–1234. https://doi.org/10.1016/j.jallcom.2018.10.136
39. M. Górny, E. Tyrała, Effect of cooling rate on microstructure and mechanical properties of thin-walled ductile iron castings, Journal of Materials Engineering and Performance, 22 (2013) 300–305. https://doi.org/10.1007/s11665-012-0233-0
40. R. Salazar, M. Herrera-Trejo, M. Castro, J. Méndez, J. Torres, M. Méndez, Effect of Nodule Count and Cooling Rate on As-Cast Matrix of a Cu-Mo Spheroidal Graphite, 8 (1999) 325-329. https://doi.org/10.1361/105994999770346873
41. A. Sadjghzadeh Benam, Effect of alloying elements on austempered ductile iron (ADI) properties and its process: Review, China Foundry, 12, (1) (2015) 54–70.
42. P. Sellamuthu, D.G. Harris Samuel, D. Dinakaran, V.P. Premkumar, Z. Li, S. Seetharaman, Effect of nickel content and austempering temperature on

microstructure and mechanical properties of austempered ductile iron (ADI), IOP Conference Series: Materials Science and Engineering, February 24-26, Bangkok, Thailand. 2018, 1–7.
https://doi.org/10.1088/1757-899X/383/1/012069

43. K.M. Pedersen N. Tiedje, Solidification of Hypereutectic thin wall ductile cast iron, Materials Science Forum, 508 (2006), 63–68.
https://doi.org/10.4028/www.scientific.net/MSF.508.63
44. S.C. Murcia, E.A. Ossa, D. J. Celentano, Nodule evolution of ductile cast iron during solidification, Metallurgical and Materials Transactions B: Process Metallurgy and Materials Processing Science, 45 (2014) 707–718.
https://doi.org/10.1007/s11663-013-9979-5
45. M. Bjerre, N.S. Tiedje, J. Thorborg, J.H. Hattel, Modelling the solidification of ductile cast iron parts with varying wall thicknesses, IOP Conference Series: Materials Science and Engineering June 21-26, Hyogo, Japan, 2015, 1-8.
https://doi.org/10.1088/1757-899X/84/1/012038
46. O.A. Tchaykovsky, O.V. Klok, Ductile cast iron induction Re-Melting, International Journal of Engineering Research & Technology (IJERT), 4 (7) (2015) 836-841.
47. Vaško, Evaluation of Shape of Graphite Particles in Cast Irons by a Shape Factor, Materials Today: Proceedings, 3 (4) (2016) 1199-1204.
https://doi.org/10.1016/j.matpr.2016.03.006
48. R.E.L. Ruxunda, D.M. Stefanescu, T.S. Piwonka, Quantification of the solidification microstructure of ductile iron through Image analysis, Proc. Of the International Conference on the Science of Casting and Solidification, January, Brasov, Romania, 2001, 361-368.
49. J.M. Bojarro, R.A. Martínez, R.E. Boeri, J.A. Sikora, Shape and count of free graphite particles in thin wall ductile iron castings, ISIJ International, 42 (3) (2002) 257-263.
https://doi.org/10.2355/isijinternational.42.257
50. S. Toraman, T. Cosgun, B. Alkan, B. Cetin, O. Akyildiz, Assessing the volume fractions of the phases, nodularity and nodule count of spheroidal graphite cast iron using Imagej software, Mugla Journal of Science and Technology, 5 (1) (2019) 137–142.
https://doi.org/10.22531/muglajsci.521128
51. P.H. Agarwal, M. Mamta, P. Patel, Effect of magnesium as spherodizer on graphite morphology in ductile cast iron, International Journal of Advance Engineering and Research Development, 3 (2) (2016) 60-63.
52. M. Holtzer, M. Górny, and R. Dańko, Microstructure and Properties of Ductile Iron and Compacted Graphite Iron Castings, Springer, Heidelberg, New York, Dordrecht, London, 2015, 109-121
53. Jh. Liu, Js. Yan, Xb. Zhao, Bg. Fu, Ht. Xue, Gx. Zhang, Ph. Yang, Precipitation and evolution of nodular graphite during solidification process of ductile iron, China Foundry, 17 (4) (2020) 260–271.
https://doi.org/10.1007/s41230-020-0042-2

54. M. Riebisch, B. Pustal, and A. Bührig-Polaczek, Influence of Carbide-Promoting Elements on the Microstructure of High-Silicon Ductile Iron, International Journal of Metalcasting, (14) (2020) 1152–1161. https://doi.org/10.1007/s40962-020-00442-1
55. G.F. Vander Voort, Metallography Principles and practice, ASM International, USA, 1999, 411-414.
56. E. Ghassemali, J.C. Hernando, D.M. Stefanescu, A. Doiszegi, A.E.W. Jarfors, J. Dluhos, M. Petrenec, Revisiting the graphite nodule in ductile iron, Scripta Materialia, 161 (2019) 66–69. https://doi.org/10.1016/j.scriptamat.2018.10.018
57. K.L. Hayrynen, The Production of Austempered Ductile Iron (ADI), 2002 World Conference on ADI, September 26-27, Kentucky, USA, 2002, 1-6.
58. W. C. Johnson, B. V Kovacs, The Effect of Additives on the Eutectoid Transformation of Ductile Iron, Metallurgical Transactions A, 9 (1976) 219-229. https://doi.org/10.1007/BF02646704
59. J. Lacaze, J. Sertucha, and L. Magnusson Åberg, Microstructure of as-cast ferritic-pearlitic nodular cast irons, ISIJ International, 56 (9) (2016) 1606–1615. https://doi.org/10.2355/isijinternational.ISIJINT-2016-108
60. W. Arshad, A. Mehmood, M.F. Hashmi, O.U. Rauf, The effect of increasing silicon on mechanical properties of ductile iron, Journal of Physics: Conference Series, 1082 (2018) 1-6. https://doi.org/10.1088/1742-6596/1082/1/012059
61. R. A. Gonzaga, Influence of ferrite and pearlite content on mechanical properties of ductile cast irons, Materials Science and Engineering: A, 567 (2013) 1–8. https://doi.org/10.1016/j.msea.2012.12.089
62. A. Javaid, J. Thomson, M. Sahoo, K.G. Davis, Factors affecting the formation of carbides in thin wall DI castings, AFS transactions, 74 (1999) 441-456.
63. M. Caldera, G.L. Rivera, R.E. Boeri, J.A. Sikora, Precipitation and dissolution of carbides in low alloy ductile iron plates of varied thickness, Materials Science and Technology, 21 (10) (2005) 1187–1191. https://doi.org/10.1179/174328405X62242
64. M. Rezvani, R. A. Harding, J. Campbell, The effect of vanadium in as-cast ductile iron, International Journal of Cast Metals Research, 10 (1) (1997) 1–15. https://doi.org/10.1080/13640461.1997.11819213
65. I. Minkoff, Alloy cast iron systems, The Physical metallurgy of cast iron, Jhon Wiley and Sons Ltd., Norwich, England, 1983, 185-188.
66. A. Cruz Ramírez, E. Colin García, J.F. Chávez Alcalá, J. Téllez Ramírez, A. Magaña Hernández, Evaluation of CADI Low Alloyed with Chromium for Camshafts Application, Metals, 12 (249) (2022) 1-24. https://doi.org/10.3390/met12020249
67. W.D. Callister Jr, Materials science and engineering an Introduction, John Wiley and Sons Ltd., USA, 2007, 291.

68. E. Guzel, C. Yuksel, Y. Bayrak, O. Sen, A. Ekerim, Effect of section thickness on the microstructure and hardness of ductile cast iron, Metallography and Hardness Measurements, 56 (4) (2014) 285–288. https://doi.org/10.3139/120.110558
69. J.M. Radzikowska, Effect of specimen preparation on evaluation of cast iron microstructures, Materials Characterization, 54 (4-5) (2005) 287–304. https://doi.org/10.1016/j.matchar.2004.08.019

List of Figures

List of Tables